Selection for targeted therapy resistance leads to an indirect selection for higher phenotypic plasticity and enhanced evolvability to orthogonal stressors

Alicia Bjornberg[1,2*], Aobuli Xieraili[1*], Matthew Froid[2,3], Rowan Barker-Clarke[4], Jeff Maltas[4], Robert Vander Velde[5], Jamir Riffas[2], Berkley Gryder[6], Alexander RA Anderson[3], David Bassanta[3], Jacob Scott[4], Virginia A Turati[3,7+], Andriy Marusyk[1+]

1. Department of Tumor Microenvironment and Metastasis, H Lee Moffitt Cancer Center and Research Institute, Tampa, FL, USA
2. Department of Molecular Biosciences, University of South Florida, Tampa, FL, USA
3. Department of Integrated Mathematical Oncology, H Lee Moffitt Cancer Center and Research Institute, Tampa, FL, USA
4. Department of Translational Hematology and Oncology Research, Cleveland Clinic, Cleveland, OH, USA
5. Department of Bioengineering, School of Engineering and Applied Sciences, University of Pennsylvania, Philadelphia, PA, USA
6. Department of Genetics and Genome Sciences, Case Western Reserve University, Cleveland, OH, USA
7. Division of Molecular Medicine and Gene Therapy, Lund University, Lund, SE

*, + Equal contribution

Corresponding Author Contacts: andriy.marusyk@moffitt.org; virginia.turati@med.lu.se

The authors declare no potential conflicts of interest.

ABSTRACT

Acquired resistance to targeted therapies is a primary barrier to durable cancer control. Resistance frequently coincides with stem-like features and EMT-associated cell-state changes (partial EMT), yet whether these programs directly cause resistance or instead enable escape by increasing phenotypic plasticity remains debated. Integrating computational modeling, functional experimental assays, and lineage tracing, we investigated how cell-state plasticity shapes acquired resistance to ALK inhibition in ALK+ lung cancer models. Our results support a model in which drug exposure selects for cells with higher phenotypic plasticity, progressively increasing their representation as resistance emerges. Consequently, resistant populations show enhanced capacity to adapt to orthogonal therapeutic and environmental stressors and exhibit heightened metastatic potential. Bulk ATAC-seq showed that highly plastic cells have increased chromatin accessibility at regulators of EMT and stemness. Consistent with this, boosting plasticity via Yamanaka-factor induction or EMT-factor expression reduced ALKi sensitivity over time. In contrast, constraining plasticity (SOX2 knockdown or epigenetic inhibition)

reduced long-term resistance outgrowth and prolonged ALKi response. Together, our results indicate that targeted therapy indirectly selects for cells with increased phenotypic plasticity, providing the substrate from which multifactorial resistance and metastatic competence evolve. Further, it suggests that constraining plasticity could delay resistance and extend response durability.

INTRODUCTION

Targeted therapies, particularly small-molecule inhibitors designed to exploit oncogenic signaling dependencies, have transformed the treatment landscape for advanced cancers[1–3]. In subsets of patients, these agents induce profound and durable initial responses. However, in most cases, these agents fail to eradicate disease, and residual cells eventually acquire resistance, leading to relapse[4]. Defining the principles that govern resistance emergence is therefore essential for extending response durability.

Mechanistically, acquired resistance has traditionally been framed as a mutational problem: on-target mutations that limit the drug binding or off-target mutations that activate bypass signaling restore proliferation in the presence of drug[5]. Yet many tumors relapse without an immediately identifiable dominant resistance driver, suggesting that resistance can involve non-genetic, cell-state adaptations in addition to canonical genetic routes[6,7]. Across systems, therapy exposure is accompanied by reversible transcriptional and chromatin remodeling, often coupled to stress-response programs, creating a permissive backdrop from which more stable resistant phenotypes can emerge over time[8–10].

In our prior work with experimental models of ALK-positive non-small lung cancers (ALK+ NSCLC), we found that resistance accrued through a multifactorial combination of genetic and non-genetic adaptations within the same cells, following inhibitor-specific trajectories in adaptive and epigenetic landscapes rather than a single dominant resistance event [11]. Similar multi-step resistance trajectories have been reported in independent systems [12,13].

These state-based models intersect with broader programs linked to plasticity, including EMT- and stemness-associated transcriptional networks (henceforth EMT/stemness), which have been repeatedly observed in resistant tumors and metastasis[14,15]. EMT/stemness signatures are often interpreted as proximal resistance mechanisms[16–18]; however, we previously showed that experimentally activating EMT is insufficient to confer complete resistance[12], motivating the alternative possibility that these programs mark increased capacity for adaptive cell-state transitions, particularly in settings where resistance emerges gradually through multiple adaptations.

To dissect the relationship between plasticity and adaptive capacity, we combined *in silico* modeling with molecular and functional analyses of therapy-naïve and therapy-resistant NSCLC cells. We show that acquired ALK inhibitor (ALKi) resistance is accompanied by broader ability to adapt to orthogonal pharmacological and environmental stressors and by increased metastatic potential.

Our data supports a model in which this broader adaptability stems from indirect selection for increased phenotypic plasticity under therapeutic pressure. We further show that this effect is most pronounced when resistance evolves through a multifactorial, stepwise trajectory. In line with this, adaptive potential can be increased or reduced by genetic and pharmacological perturbations. Together, these results suggest that limiting phenotypic plasticity may prolong response durability by delaying resistance emergence.

RESULTS

Independent ALKi resistance trajectories converge on EMT/stemness and cross-stressor adaptability

Our previous work in an experimental model of ALK+ NSCLC showed that the development of resistance to clinically relevant concentrations of multiple ALKi is characterized by the gradual accumulation of resistance-conferring molecular changes. Whereas mutational changes contributed to this process, adaptation was dominated by expression-level, epigenetic changes. Surprisingly, even though resistance to any given ALKi was associated with cross-resistance to different ALKi, evolution of resistance to distinct ALK inhibitors was characterized by predictively distinct, inhibitor-specific evolutionary trajectories, and mediated by distinct combinations of resistance-promoting mechanisms[11]. Building on these experiments, we asked, despite these differences, whether there is a common denominator to ALKi resistance. To this end, we focused on resistance to the two most clinically relevant ALKi, alectinib and lorlatinib. In our experiments, resistant variants of the H3122 cell line were derived by continuous exposure to clinically relevant drug concentrations until stable resistance emerged, yielding lorlatinib-evolved (erLor) or alectinib-evolved (erAlec) resistant cells (collectively erALKi) (**Fig. 1A**).

Notably, erALKi cells displayed a more mesenchymal morphology compared to their treatment-naïve counterparts (**Fig. 1B**). Further, transcriptomic profiling and gene set enrichment analysis (GSEA) showed that erAlec and erLor cells shared activation of TNF-α and TGF-β signaling (**Fig. 1C–D, Fig. S1A–B**), pathways implicated in EMT, stemness, and metastasis[19–25]. While EMT is often considered to be a direct resistance mechanism[16–18], our previous studies demonstrated that EMT induction, per se, have modest to negligible effect on drug sensitivity in common cell viability assays[12]. Given the association of intermediate

106 EMT with higher phenotypic plasticity and stemness, we hypothesized that the convergent
107 EMT-enrichment in erALKi cells might reflect selection for cells with higher capability of
108 undergoing adaptive cell-state transitions under sustained therapeutic selection
109 pressures.

110 To test this hypothesis, we first asked whether erALKi cells display higher transcriptional
111 entropy, which can be captured with the Gini index, a metric previously used to
112 quantitatively infer differentiation potential and plasticity in normal and cancer stem
113 cells[26,27]. Indeed, erALKi cells exhibited significantly higher entropy compared with
114 treatment-naïve cells, consistent with the elevated EMT/stemness (**Fig. 1E**). Next, we
115 sought to evaluate our hypothesis more directly in a functional assay. We reasoned that if
116 EMT reflects a higher plasticity cell state, the erALKi cells should be more capable of
117 adapting to orthogonal stressors, without necessarily showing higher fitness in short term
118 assays. In this case, adaptability can be distinguished from intrinsic resistance by
119 contrasting the initial sensitivity of therapy-naïve and erALKi cells to orthogonal stressors,
120 with their sensitivity after prolonged incubation under stress once cells have had an
121 opportunity to adapt. In this experimental design, higher plasticity-mediated adaptive
122 potential could be identified as a higher viability in long-term, but not short-term assays
123 (**Fig. 1F**).

124 We started by contrasting short- and long-term sensitivity of erALKi and naïve H3122 cells
125 to microenvironmental stresses commonly encountered within tumors: hypoxia, acidosis,
126 and nutrient starvation[28,29]. After short-term exposure (3 days), resistant and naïve cells
127 showed similar survival and growth, indicating that EMT does not confer an intrinsic
128 resistance to these stressors. However, the prolonged exposure (≥10 days; specific
129 duration chosen based on the stressor-specific adaptation timelines), erALKi cells
130 displayed markedly higher viability (**Fig. 1G**), consistent with a higher adaptive potential**.**
131 Next, we asked whether erALKi cells are more capable of adapting to clinically relevant
132 orthogonal signaling inhibitors targeting MEK1/2 (trametinib), JAK1/2 (ruxolitinib), and
133 mTOR (rapamycin)[30–33]. Similar to the observations with environmental stressors, while
134 early responses were comparable, resistant populations progressively adapted and
135 displayed increased growth relative to naïve cells (**Fig. 1H, Fig. S1C**). These data show that
136 EMT phenotypes of erALKi cells are associated with a generalized, time-dependent
137 capacity to adapt to unrelated pharmacological and environmental stressors, rather than
138 an intrinsic resistance to orthogonal stressors.

139 We next asked whether this adaptive potential extends to an enhanced ability to adapt to
140 new tissue environments. Metastatic colonization represents a stringent selective
141 bottleneck that requires plasticity-mediated adaptation[34]. To test whether ALKi resistant

142 states exhibit broader adaptive capacity, we injected 1:1 mixtures of mCherry-labeled
143 resistant cells (erLor or erAlec) and GFP-labeled naïve cells subcutaneously into the flanks
144 of NSG mice. While the primary tumors maintained the initial 1:1 ratio, consistent with the
145 lack of engraftment and growth differences between naïve and erALKi cells, analysis of
146 spontaneous lung metastases by fluorescence-activated cell sorting (FACS) revealed
147 enrichment of resistant cells, with two-fold more mCherry+ (erLor and erAlec) than GFP+
148 (naïve) cells recovered from metastatic lesions (**Fig. 1I**). Control mice injected with naïve
149 cells alone and comparable flank engraftment excluded fluorophore bias and differences
150 at the primary site, indicating that enrichment was specific to the metastatic setting. To
151 distinguish between enhanced dissemination from the primary tumor versus superior
152 adaptability at the metastatic site, we bypassed local invasion and intravasation by
153 injecting resistant and naïve cells directly into the circulation via the tail vein[35]. Resistant
154 cells again outcompeted naïve cells by two- to three-fold in lung colonization (**Fig. 1J, Fig.
155 S1D**), demonstrating that resistant cells adapt more effectively to the lung
156 microenvironment, a property consistent with enhanced plasticity.

157 Together, these data show that ALK inhibitor resistance converges on EMT/stemness-
158 associated programs, characterized by increased transcriptional entropy and a higher
159 capacity for adaptation towards orthogonal stressors and new tissue contexts.

160 **Multi-step resistance dynamics predict progressive enrichment of rare high-plasticity
161 cells**

162 The convergence of ALKi resistance on phenotypes characterized by elevated phenotypic
163 plasticity suggests that selection for ALKi resistance leads to indirect selection for
164 enhanced phenotypic plasticity. We speculated that this strong convergence might reflect
165 the complexity and multifactorial nature of resistance dynamics revealed in our recent
166 studies[11,12], where a multitude of steps towards resistance might strongly amplify the
167 indirect selection for higher adaptability. To test this prediction, we developed an *in silico*
168 model of heterogeneous tumor populations contrasting the selective advantage of
169 increased adaptability under single-hit and multi-step resistance acquisition scenarios
170 (**Fig. 2A**).

171 To capture both spatial and well-mixed dynamics, we used two approaches: a spatial
172 agent-based model (ABM) (**Fig. S2A**) and a non-spatial ordinary differential equation (ODE)
173 model (**Fig. S2B–C**, **Supplementary Methods**). In both ABM and ODE implementations,
174 cells differed in an abstract plasticity parameter that sets the probability of developing
175 phenotypic changes that increase fitness under treatment. Cells could transition towards
176 fitter resistant states stochastically, allowing us to track subpopulation dynamics under
177 treatment over time.

178 In our simulations we sought to recapitulate a scenario of therapeutic responses of a
179 therapeutically sensitive neoplastic population composed of cells with varying adaptation
180 potential. Of the 10,000 cells initialized in the simulation, the majority (90%) are incapable
181 of adaptation (phenotypic-change rate = 0); these are meant to reflect cells that are
182 effectively eliminated by therapy. The remaining 10% are capable of acquiring resistance-
183 promoting adaptations: 9% exhibit baseline adaptability (1x change rate), while just 1%
184 exhibit higher adaptability (2x change rate) (**Fig. 2B**). The relatively modest difference in
185 phenotypic change rates was chosen deliberately; as larger differences should inevitably
186 amplify the expected effects. At each step, cells could die, divide, or undergo a phenotypic
187 change representing cumulative genetic and/or epigenetic modifications without
188 specifying molecular origin (**Fig. 2B**). Key parameters were systematically varied, including
189 the initial frequencies of plastic subpopulations and the nature of treatment applied. We
190 modeled cytostatic therapy by reducing proliferation (**Fig. S2B**) and cytotoxic therapy by
191 increasing death (**Fig. S2C**).

192 Whereas partial selection for cells with higher plasticity potential was observed under the
193 single-hit scenario, these resistant populations were dominated by the descendants of the
194 initially more numerous cells with baseline plasticity. In contrast, across parameter
195 regimes, the multi-step framework progressively enriched subpopulations with elevated
196 plasticity (**Fig. 2C, Fig. S2A–D**). Together, our *in silico* simulations indicate that i) evolution
197 of resistance is associated with an indirect selection for cells with higher adaptability
198 potential and ii) that this selection is strongly augmented under a scenario of multi-step
199 resistance.

200 **Individual NSCLC clones can be classified into adaptation potentials with distinct**
201 **functional and molecular profiles**

202 Next, we sought to examine the existence of empirical evidence for the simulation's key
203 assumption, that treatment-naïve populations contain rare lineages with elevated
204 adaptability. To this end, we performed high-complexity lineage tracing using two
205 independent DNA barcode libraries (CloneTracer[36] and CloneSweeper[37]). Each barcoded
206 population was challenged with a panel of kinase-pathway inhibitors and
207 microenvironmental stressors (**Fig. 2D**). Barcode composition before and after each
208 challenge was compared, and enrichment relative to baseline composition was used to
209 identify lineages that expanded across conditions.

210 Across both libraries, we observed a rare subset of barcodes that expanded under multiple
211 conditions, with partial reproducibility across replicates, consistent with stochastic
212 selection and context-dependent adaptive solutions rather than a single fixed "winner"
213 lineage (**Fig. 2E, Fig. S3A–D**). Specifically, we observed reproducible structure in which

214 stressors tend to co-select overlapping sets of lineages. For example, in one dataset,
215 barcodes enriched under ceritinib, crizotinib, lorlatinib, and brigatinib clustered separately
216 from those enriched under alectinib and trametinib, or low pH and nutrient starvation (**Fig.**
217 **S3B**). In the other library, barcodes selected by alectinib and lorlatinib were grouped apart
218 from those expanded under acidic conditions (**Fig. S3D**). While our lineage tracing
219 experiments indicate a complex scenario where distinct subpopulations vary in their ability
220 to adapt to distinct stressors, they also support the notion of existence of a subpopulation
221 of cells with an enhanced general adaptability within therapy-naïve H3122 cells.

222 To test for this inference more directly, we derived single-cell clones from treatment-naïve
223 H3122 cells (**Fig. 3A**) and contrasted their ALKi adaptation potential. Using flow sorting, we
224 seeded single cells into individual wells of 96-well plates and verified single-cell seeding by
225 microscopy. From 127 sorted cells, 21 clonal colonies were established and then
226 challenged independently with clinically relevant concentrations of ALK inhibitors
227 (alectinib, lorlatinib, crizotinib, ceritinib, brigatinib). Clonal responses were quantified
228 using long-term clonogenic outgrowth assays after sustained drug exposure, with resistant
229 colonies visualized by crystal violet staining (**Fig. 3B-C**). Whereas baseline proliferation and
230 short-term ALKi sensitivity showed no substantial variability, long-term clonogenic
231 outgrowth varied markedly across clones, revealing clear differences in the ability to adapt
232 under continued ALK inhibition (**Fig. 3D, Fig. S4A-B**). Two clones capable of clonogenic
233 outgrowth across all ALKi were denoted high adaptation-potential (HAP). Eleven clones
234 that failed to establish colonies under any ALKi were denoted low adaptation-potential
235 (LAP). The remaining eight clones displayed intermediate behavior, with clonogenic
236 outgrowth under some but not all ALKi, and were denoted intermediate adaptation-
237 potential (IAP). This distribution is consistent with our barcoding data and prior reports
238 indicating that resistance originates from a rare fraction of the therapy-naive tumor cell
239 populations[6,11,12,36].

240 To test whether the adaptation phenotypes were stable over time in culture, naïve LAP, HAP,
241 and parental cells were passaged and plated weekly into clonogenic assays (**Fig. S4C**).
242 Cells were then treated with ALKi for four weeks to allow resistant colony formation,
243 followed by crystal violet staining and quantification. The phenotypes remained stable over
244 eight weeks of passaging: HAP clones consistently formed larger and more numerous
245 resistant colonies, whereas LAP clones failed to generate colonies under ALKi (**Fig. S4D**).
246 The parental population formed colonies at intermediate frequency, as expected from a
247 heterogeneous mix of lineages. These results demonstrate that the observed differences in
248 adaptation potential are stable over extended culture and are not altered by routine serial
249 passaging.

250 Next we asked whether the variability in ALKi adaptation potential extends towards *in vivo*
251 responses. To this end, xenograft tumors were generated from LAP and HAP cells and
252 subcutaneously implanted into NSG mice. Consistent with the *in vitro* assays, we did not
253 observe differences in the initial alectinib responses between LAP and HAP xenografts.
254 However, around 8 weeks of treatment responses started to diverge, with HAP tumors
255 developing resistance while LAP tumors continued to regress (**Fig. 3E**). To assess whether
256 LAP tumors were fully eliminated, the treatment was discontinued at week 21. Treatment
257 discontinuation triggered tumor relapse, indicating the survival of viable tumor cells within
258 microscopic residual disease. After relapsing tumors reached pre-treatment sizes,
259 alectinib treatment was resumed. Notably, relapsed tumors displayed strong responses,
260 similar to the responses of treatment-naïve LAP tumors, indicating that LAP tumor cells
261 failed to develop measurable resistance (**Fig. 3E**).

262 We then asked whether the enhanced ALKi adaptive potential of HAP cells reflected an
263 enhanced adaptability in general. To this end, we used our functional assay pipeline and
264 panel of orthogonal stressors initially developed to uncover the enhanced adaptability
265 potential of ALKi cells (**Fig. 1F-H**). We found that while the initial sensitivity of HAP cells to
266 orthogonal stressors was similar to the sensitivity of LAP, IAP and parental cells, the HAP
267 cells were more capable of developing resistance over time (**Fig. 4A-B**). Finally, we asked
268 whether, similar to ALKi cells, HAP cells are more capable of metastatic colonization. To
269 this end, LAP, HAP, and parental cells were engineered to express Cypridina luciferase[38],
270 enabling longitudinal vital monitoring of metastatic burden after tail-vein injection (**Fig.
271 4C**). Within two weeks, the luciferase signal dropped below the detectability threshold in
272 all of the injected mice, consistent with the expectation of substantial selection
273 bottleneck. By 15 weeks, all mice injected with HAP cells exhibited strong luciferase signal,
274 indicating outgrowth of metastatic tumors, whereas plasma luciferase levels in LAP-
275 injected mice remained below the detection threshold (**Fig. 4D**). Parental cells displayed
276 an intermediate phenotype: whereas 3/4 injected animals had detectable luciferase signal,
277 the kinetics were delayed compared to HAP cells (**Fig. 4D**), consistent with their
278 heterogenous composition containing only a minority of high adaptation-potential clones.
279 Examination of tissues at point of euthanasia validated presence of macroscopic lung and
280 liver tumors in the animals with detectable luciferase signals (**Fig. S6A**), while no
281 detectable tumors were observed in animals seeded with LAP cells. Together, these results
282 support the notion that therapy-naïve tumor cells contain subpopulations with an
283 increased general adaptation potential.

284 **Chromatin accessibility informs therapeutic vulnerabilities to modulate adaptation
285 potential**

286 To identify the mechanistic underpinning of differences in the adaptive potential, we
287 started with characterization of transcriptional programs. To this end, we performed bulk
288 RNA-seq on LAP, IAP, and HAP clones. Unsupervised clustering and PCA grouped clones by
289 class (**Fig. S5A–B**), indicating that LAP/IAP/HAP subpopulations correspond to stable,
290 molecularly distinct transcriptional states. LAP clones showed the greatest inter-class
291 heterogeneity, whereas HAP clones displayed more consistent profiles. GSEA revealed
292 that, similarly to cells with evolved resistance, HAP clones upregulated EMT- and
293 stemness-associated pathways, including TGF-β, Hedgehog, and TNFα/NF-κB (**Fig. 4E, Fig.**
294 **S5C**)[19–25,39]. Consistent with these profiles, LAP clones retained the rounded cobblestone
295 morphology of parental cells, whereas HAP clones displayed a more mesenchymal
296 phenotype (**Fig. S5D**).

297 Chromatin accessibility can shape adaptation by regulating transcriptional responses to
298 environmental change[40]. To test whether adaptation potential is associated with a distinct
299 regulatory landscape we next profiled chromatin accessibility by bulk ATAC-seq[41]. HAP
300 cells displayed increased accessibility at developmental, cell-identity regulators, and
301 enrichment of EMT/stemness-associated motifs, including KLF4 and SOX family members
302 (**Fig. 5A–B**, **Fig. S6B-C**). Whereas the reading depth of our bulk RNA seq analyses was
303 insufficient to detect the expression of these transcriptional factors, the ATAC-seq analyses
304 support the notion that the enhanced expression of EMT programs in HAP clones is
305 associated with higher stemness.

306 We next tested whether adaptation potential can be shifted in either direction by perturbing
307 cell-state regulators. To increase adaptation potential in LAP cells, we induced stemness
308 via expression of Yamanaka factors (Oct4, SOX2, KLF4, c-MYC; OSKM)[42] and, in parallel,
309 induced EMT via overexpression of Slug (SNAI2)[12,43–46]. In both cases, these manipulations
310 reduced sensitivity to ALKi over time in long-term assays (**Fig. 5C**) and were accompanied
311 by a morphological shift toward a more mesenchymal phenotype (**Fig. S6D**), consistent
312 with increased capacity to adapt under sustained drug challenge.

313 Conversely, we tested whether the high adaptation-potential phenotype could be
314 dampened by limiting plasticity-associated regulators in HAP cells. Guided by our ATAC-
315 seq results, which showed increased accessibility and motif enrichment for SOX family
316 regulators in HAP cells, we performed shRNA-mediated knockdown of SOX2 (**Fig. S6E**).
317 SOX2 knockdown did not restore acute ALKi sensitivity or alter short-term growth, but it
318 significantly reduced the capacity to develop resistance in long-term assays (**Fig. 5D**).
319 Together, these bidirectional perturbations show that adaptation potential is
320 experimentally modifiable, enhanced by enforcing stemness/EMT programs in LAP cells

321 and reduced by limiting a plasticity-sustaining regulator in HAP cells, with corresponding
322 effects on long-term resistance emergence (**Fig. 5C–D**).

323 Although direct pharmacological targeting of transcriptional factors is currently not
324 feasible, because HAP and LAP cells show comparable short-term sensitivity to ALKi, we
325 hypothesized that epigenetic inhibitors could limit adaptive phenotypic cell state
326 transitions in HAP cells; thereby locking them in a drug-sensitive state. To test this, we
327 treated HAP cells with either the histone deacetylase (HDAC) inhibitor panobinostat[47,48] or
328 the histone acetyltransferase (HAT) inhibitor A485[49]. Doses were selected to avoid direct
329 cytotoxicity while producing a measurable stress response, as reflected by decreased
330 NRF2 (*NFE2L2*) expression (**Fig. S6F**). Cells were then plated into ALKi either untreated,
331 after 7-day pretreatment with an epigenetic inhibitor, or under continuous co-treatment
332 with epigenetic inhibitor plus ALKi (**Fig. S6G**). In both pretreated and co-treated groups,
333 panobinostat prolonged ALKi sensitivity, whereas untreated HAP cells eventually started
334 re-growing (**Fig. 5E**). A485 produced similar effects (**Fig. S6H**), consistent with prior reports
335 that both HDAC and HAT inhibitors can restrict expression of core regulatory transcription
336 factor genes[50]. These findings indicate that pharmacologic interference with chromatin
337 regulators can suppress the ability of tumor cells to adapt to pharmacological stressors.

338 Together, these experiments show that phenotypic plasticity is reflected in chromatin
339 accessibility, can be increased or constrained genetically, and can be pharmacologically
340 restrained. By showing that resistance evolves not solely from pre-existing, intrinsically
341 resistant clones but through progressive selection of rare, highly plastic cells, our findings
342 redefine how therapeutic pressure sculpts tumor evolution and point to plasticity itself as a
343 central, targetable driver of resistance.

344 **DISCUSSION**

345 Across cancers, acquired resistance to targeted therapy has been linked to EMT- and
346 stemness-associated programs, increased metastatic potential, and tolerance to
347 chemotherapy and radiotherapy[51]. Here we show that these recurring features can be
348 understood through a common principle: targeted therapy selects for subpopulations with
349 higher phenotypic plasticity, and this plasticity, rather than a single resistance pathway,
350 drives delayed, multifactorial escape and metastatic competence. We define plasticity as
351 an expanded capacity for therapy-induced state transitions that enables populations to
352 discover adaptive solutions over time. Importantly, this does not necessarily require that
353 highly plastic cells are intrinsically rare at baseline: resistance would be expected to
354 emerge faster when a larger fraction of cells can enter plastic states, and plasticity itself
355 can be induced or amplified by therapeutic and microenvironmental stress.

Our *in silico* model formalized two alternative evolutionary frameworks and predicted that multi-step resistance should progressively enrich subclones with higher plasticity, including when they are scarce at baseline. A key implication was that fitness differences would be largely invisible early during treatment and instead emerge as a delayed expansion of the plastic compartment with continued exposure. Our experiments recapitulated these population-level dynamics: lineage barcoding and single-cell–derived clones revealed a pretreatment fraction with higher adaptation potential that expanded under sustained pressure. Lineage tracing also suggests additional complexity: enrichment profiles were overlapping but not identical across challenges and replicates, consistent with subpopulations that are more capable of adapting to specific stressors, as well as a component of pre-adaptation present before exposure. Here, we focus on plasticity-mediated adaptability across challenges as a general route by which therapeutic pressure can drive resistance evolution. Short-term responses were similar across lineages, but over longer intervals, the high adaptation-potential fraction recovered, adapted to pharmacologic and microenvironmental stressors, and colonized the lung more efficiently *in vivo*.

This selection-for-plasticity framework refines how EMT and stemness should be interpreted in the context of resistance. Rather than serving as universal proximal mechanisms of escape, EMT- and stemness-associated programs mark, and can facilitate, a broader plasticity state that widens the repertoire of phenotypes accessible under selection. In settings where state transitions occur rapidly, plasticity-driven escape may appear as an immediate resistance mechanism, but our data support a time-dependent process in which adaptability emerges through continued selection and reconfiguration. Consistent with this view, the high adaptation-potential fraction shows increased transcriptional entropy and preferential chromatin accessibility at developmental and cell-identity regulators, features consistent with a regulatory architecture that can be reconfigured under treatment. Importantly, perturbing these identity programs altered long-term outcomes without changing immediate drug sensitivity: partial reprogramming or EMT induction increased adaptation potential in low-plasticity clones, whereas limiting plasticity-sustaining transcription factors reduced resistant outgrowth over longer intervals. Together, these results support plasticity as a convergent, targetable early step on the path to resistance and show that genetic or pharmacologic interventions that constrain plasticity can shift the timing and likelihood of escape.

Although our experiments emphasize non-genetic adaptation, the same principle can extend to settings where resistance is ultimately driven by genetic alterations. By expanding the phenotypic space on which selection operates, plasticity can facilitate reversible reconfiguration and create opportunities for genetic changes that stabilize fitter states. This

393 perspective reconciles drug-specific molecular heterogeneity with recurrent convergence
394 on shared functional properties. Distinct ALK inhibitors drive divergent transcriptional
395 states, yet resistant populations display cross–ALK inhibitor tolerance together with
396 EMT/stemness features, consistent with selection acting on plasticity in addition to drug-
397 specific pathways.

398 Clinically, progression on targeted therapy is frequently followed by attenuated benefit
399 from subsequent cytotoxic chemotherapy, consistent with resistant disease acquiring
400 broader stress tolerance rather than escaping through a single drug-specific route[52–54].
401 Resistance also commonly coincides with metastatic progression, and a prevalent
402 interpretation is that this reflects simple arithmetic. Longer disease duration and larger
403 tumor burden provide increased opportunities for dissemination. However, this framing
404 does not explain why resistant disease so often becomes broadly robust across therapies
405 and environments. Our results instead suggest a plausible mechanistic connection:
406 selection for phenotypic plasticity under sustained therapeutic pressure can promote
407 cross-stressor tolerance and increase the likelihood of successful growth in new tissue
408 contexts.

409 Local microenvironmental constraints are likely to modulate both the emergence and the
410 consequences of this plasticity. Hypoxia, acidosis, nutrient limitation, and paracrine
411 signaling through pathways such as TGF-β and NF-κB can remodel chromatin and redirect
412 transcriptional programs, thereby modulating plasticity and the probability of adaptation[55–
413 57]. Consistent with niche effects, we observe heterogeneity between sites: enrichment
414 patterns differ between primary and metastatic settings, and resistant/high-plasticity cells
415 show superior lung colonization relative to naïve counterparts.

416 This work focuses on ALK-rearranged NSCLC in long-term culture and xenograft models.
417 Future studies should test how broadly selection for plasticity generalizes across
418 oncogenic drivers, tissues, and immune-competent settings, and should further define
419 quantitative, predictive measures of plasticity in patient samples.

420 Our findings have translational implications. If treatment selects for plasticity, then
421 intervention timing and combination strategies that constrain state switching may prolong
422 response. In our models, interventions that stabilize cell identity or restrict reprogramming
423 prolonged sensitivity to targeted inhibitors, motivating treatment schedules that intervene
424 during the period when cells begin to reprogram under therapy, before overt resistance
425 emerges. Composite biomarkers of plasticity, including entropy-based metrics,
426 EMT/stemness gene sets, motif-level chromatin signatures, and functional stress-
427 adaptation assays, could stratify risk and guide trials designed to restrain adaptive
428 reprogramming and capture delayed adaptation as an endpoint[58,59]. More broadly, viewing

429 plasticity as a rate-limiting resource provides a framework for integrating non-genetic
430 tolerance with subsequent genetic stabilization of resistant states.

431 In sum, our data support a model in which therapeutic pressure progressively enriches
432 subpopulations with higher phenotypic plasticity, and this plasticity enables time-
433 dependent adaptation, multifactorial resistance, and metastatic competence. EMT- and
434 stemness-associated programs often accompany, and can potentiate, this capacity but are
435 not, in most contexts, sufficient on their own to confer durable escape. Recognizing
436 plasticity as the trait under selection provides a coherent account of delayed resistance,
437 recurrent transcriptional convergence, and site-specific behavior, and motivates evolution-
438 informed strategies that stabilize identity, modulate paracrine drivers, and constrain
439 adaptive trajectories.

440 **METHODS**

441 **Cell culture**
442 NSCLC cell line H3122 was obtained from the Lung Cancer Center of Excellence Cell Line
443 depository at Moffitt Cancer Center. H3122 cells were grown in RPMI-1640 containing L-
444 Glutamine (Gibco), supplemented with 10% fetal bovine serum (FBS), 1% penicillin-
445 streptomycin, and 10μg/ml human recombinant insulin (Gibco). Cells were incubated at
446 37℃ with 5% CO_2 atmosphere with constant humidity. Cells were passaged as needed
447 using 0.25% trypsin (Gibco). Passage number was kept below 15 passages to maintain
448 consistency in phenotypes.
449
450 **Derivation of erLor and erAlec cells**
451 As detailed in Vander Velde (2020)[11], H3122 cells were subjected to continuous high ALKi
452 concentrations of 2.0uM alectinib or 2.0uM lorlatinib (Fisher Scientific).
453
454 **Single-cell Clones derivation**
455 H3122 cells were detached using accutase (Gibco), passed through cell strainers and
456 subjected to sterile flow sorting (BD FACSAria II) to obtain single-cell droplets into six 96-
457 well plates. After careful microscopic evaluation at 1, 3, and 5 days post sorting, we scored
458 24 wells that had growth from a single cell. Cells were further expanded to proceed with
459 experiments.
460
461 **Classification of single-cell derived clones into high, intermediate, or low adaptation**
462 **potential**
463 We assessed 21 single-cell derived clones' ability to evolve resistance to alectinib by long-
464 time drug exposure at 500nM (up to 3 months). Among the 21 subclones, 2 showed high

465 adaptation potential, 8 showed intermediate, 11 showed no adaptability scored by their
466 confluency when we stopped the experiment. In order to confirm this preliminary
467 observation and further assess their evolvability of resistance to other TKI's, duplicate
468 cultures of 10,000 cells/well from each clone seeded into 24-well plates. After 24h, media
469 was replaced with media containing 0.1% DMSO or one ALKi (0.1μM ceritinib (Fisher
470 Scientific), 0.5 μM crizotinib (FisherScientific), 0.5 μM lorlatinib, 0.5 μM alectinib, or 0.1 μM
471 brigatinib (AstaTech). After 40 days of culture, plates were subjected to crystal violet
472 staining and their growth measured by ImageJ by scoring the colony area of wells covered
473 by cells.
474
475 **Functional assays**
476 Cells were collected, counted, and plated such that the same number of cells was added
477 to each well of the experimental plate. 24 hours after seeding, media containing the
478 treatment, stressor, or vehicle was added and subsequently replaced every 3-4 days.
479 Acidosis media was made by adding HCl (6N, VWR) to RPMI-1640 until the pH reached 5.5.
480 Then the acidic media was filtered (0.2um) and the rest of the media components were
481 added. For pseudo-hypoxia media, cobalt chloride hexahydrate ($CoCl_2$) was dissolved in
482 PBS then added to RPMI complete media so the final concentration is 200uM. For
483 starvation media, when stressing the evolved resistant lines, the complete media was
484 diluted 1:10 in PBS; when stressing the single-cell derived clones, the complete media was
485 diluted 1:5 in PBS. Cell viability was assessed using crystal violet staining followed by
486 ImageJ quantification or elution, or through Cell Titer Glo assay following manufacturer
487 instructions. Short term assays lasted 3-7 days, long term assays lasted 10-30 days.
488
489 **Crystal violet staining**
490 At endpoint, the plate was placed on ice and washed with ice cold PBS (Gibco). Then the
491 cells were fixed with 100% methanol (Fisher Chemical) for 10 minutes on ice. The methanol
492 was aspirated off and the plate was placed at room temperature before 0.5% crystal violet
493 solution in 25% methanol was added for 10 minutes. The crystal violet solution was
494 removed and the plate was submerged in distilled water multiple times to remove excess
495 stain. The plate was placed upside down to dry at room temperature. Once dry, the crystal
496 violet stained plates were imaged on the Amsheran Imager 600 using the colorimetric
497 trans-illumination setting.
498
499 **Acetic Acid Elution**
500 After imaging on the Amsherham Imager 600, 10% acetic acid (Fisher Chemical BP2401-
501 500, diluted in double-distilled water) was added to each well, 50ul for a 96-well plate, or
502 200ul for a 48-well plate. The plate was placed on a shaker for 15 minutes to agitate and

503 elute the crystal violet staining. Then, the acetic acid and crystal violet mixture was diluted
504 with distilled water in a 1:4 ratio. In a new 96-well white-walled clear-bottom plate, 100ul of
505 the solution in each well of the original plate was transferred to a new well in the new plate.
506 The BioTek Synergy Microplate reader read the plate at 590nm. All values were normalized
507 to mean absorbance in DMSO.
508
509 **ImageJ quantification**
510 To analyze the image from the Amsherham Imager 600 using ImageJ, the oval selection tool
511 was used to select a single well. The image was then converted to 16-bit. Next, the
512 "Analyze" menu was used to select "Measure" to measure the entire area of the selected
513 well. Then, the "Image" menu was used to select "Adjust" followed by "Threshold." The red
514 mask is used to select empty spaces before selecting “Analyze" and "Measure" again to
515 measure the red area. Subtract the red area from the entire area which was measured first
516 to get the desired measurement.
517
518 **Cell Titer Glo Assay**
519 Cell viability was assessed using CellTiterGlo reagent (Promega) following the
520 manufacturers protocol and detected using the luminescence setting on a GloMax
521 luminometer (Promega).
522
523 **Cell imaging**
524 Brightfield images were taken on a Zeiss AXIO Observer Z1 microscope to examine cell
525 morphology. For imaging of ex vivo resistant and parental cells, fluorescent channels of
526 610nm (mCherry) and 509nm (GFP) were used to differentiate between cell lines.
527
528 **CloneTracer**
529 H3122 cells were transduced at 30% efficiency (as defined by fluorescence-activated cell
530 sorting analysis of dsRed expression) with CloneTracer neutral DNA barcode library, kindly
531 provided by Frank Stegmeier (Addgene #67267). Barcode-containing cells were selected
532 with puromycin and expanded for 7 days. Barcoded cells were collected and split into
533 conditions. Triplicate cultures of 100,000 cells each were plated into 6-well plates in the
534 presence of 0.1% DMSO, 0.5 μM crizotinib, 0.5 μM alectinib, and 0.5 μM lorlatinib, 0.1 μM
535 ceritinib, 0.1 μM brigatinib, 0.1 μM trametinib, starvation, or acidosis conditions. One
536 aliquot of 100,000 cells was frozen to serve as an initial time point. Cells were collected
537 following 4-8 weeks of cell culture based on their growth in different conditions. Genomic
538 DNA was extracted using proteinase K digest, followed by phenol–chloroform purification.
539 Barcodes were amplified, sequenced, and analyzed following protocols described in (36)
540 and an updated procedure provided on the Addgene website https://www.addgene.org/

541 pooled-library/clontracer. PCR amplification was done with the protocol provided by
542 Stegmier lab, 30 cycles using second-generation ClonTracer primers with the following
543 sequence: 5'-CAA GCA GAA GAC GGC ATA CGA GAT-Variable Sequence-GTG ACT GGA GTT
544 CAG ACG TGT GCT CTT CCG ATC TCT AGC ACT AGC ATA GAG TGC GTA GCT-3'.
545
546 **CloneSweeper**
547 H3122 cells were transduced at 5% efficiency, as defined by fluorescence-activated cell
548 sorting analysis of GFP expression, with the neutral DNA barcode library, kindly provided by
549 Shaffer Lab (37). Cells containing barcodes were cultured for 12 days and then divided into
550 treatment groups of 200,000 cells per 10 cm plate. Treatments included DMSO (0.05%),
551 lorlatinib (0.5 μM), alectinib (0.5 μM), or medium adjusted to pH 5.5. An additional aliquot
552 of 200,000 cells was frozen to serve as an initial timepoint. Four plates were prepared for
553 each treatment condition. One plate was harvested and frozen two weeks after treatment
554 initiation to look at intermediate resistance abundance, while the remaining plates were
555 collected once confluent, approximately four weeks for the pH 5.5 condition and five
556 weeks for the lorlatinib and alectinib treatments. Barcode sequences were amplified,
557 sequenced, and analyzed according to the genomic DNA barcode sequencing protocol
558 described in (37).
559
560 **Barcode enrichment analysis**
561 For each library, distinct barcode sequences and their corresponding read counts were
562 summarized and merged into a unified count matrix in R (v4.4.0). To account for differences
563 in sequencing depth, barcode counts were normalized to the total number of reads per
564 sample, yielding relative barcode abundances. The resulting normalized and raw count
565 matrices were used for enrichment and comparative evaluations. Barcodes with a
566 frequency above 0.001 in at least 2 samples were kept for further analysis.
567
568 **Lentiviral overexpression of Yamanaka factors and Slug**
569 Lentiviral vector for inducible overexpression of *Oct4, Klf4, Myc and Sox2* (OSKM; FUW-
570 tetO-hOKMS) was a gift from Tarjei Mikkelsen (Addgene #51543). Lentiviral vector for
571 inducible expression of *Slug* (Addgene #82162) was Gateway-cloned under a doxycycline
572 induced promoter on a pInducer20 backbone (Addgene #44012). JetPrime reagents and
573 protocol (Polyplus) were followed for transfection into HEK-293T packaging cells. Virus-
574 containing supernatant was collected 24-48h after transfection and filtered through
575 0.45μm filters (Corning). H3122 low adaptation-potential derivatives were infected with
576 viral lysate containing polybrene (Santa Cruz Biotechnology) before selection in the
577 appropriate antibiotic. To induce expression of either Yamanaka factors or Slug,
578 doxycycline was added to the cell medium for 30 days prior to experiment initiation.

579
580 **shRNA knockdown for SOX2**
581 SOX2 inducible lentiviral small hairpin RNA (shRNA) (Tet-pLKO-puro-SOX2) was a gift from
582 Charles Rudin (Addgene #47540). JetPrime reagents and protocol (Polyplus) were followed
583 for transfection into HEK-293T packaging cells. Virus-containing supernatant was collected
584 24-48h after transfection and filtered through 0.45μm filters (Corning). H3122 high
585 adaptation-potential derivates were infected with viral lysate containing polybrene (Santa
586 Cruz Biotechnology) before selection in the appropriate antibiotic. To induce *SOX2*
587 knockdown, doxycycline was added to the cell medium for 7 days prior to experiment
588 initiation.
589
590 **Treatment with Epigenetic Inhibitors**
591 HAP cells were pre-treated with either vehicle (DMSO) or an epigenetic inhibitor A485 (4μM,
592 MedChem Express) or Panobinostat (2 μM, Fisher) for 7 days prior to exposure to ALKi. One
593 arm was co-treated with the epigenetic inhibitor and ALKi to make a total of 3 groups: 1)
594 HAP pretreated with DMSO, then treated with ALKi, ii) HAP pre-treated with epigenetic
595 inhibitor, then treated with ALKi, iii) HAP pre-treated with DMSO, then co-treated with ALKi
596 and epigenetic inhibitor.
597
598 **PCR**
599 RNA extraction was performed with RNAeasy (Qiagen) according to the manufacturer's
600 instructions. Quantitative reverse transcriptase real-time PCR was performed using
601 SensiFAST SYBR Hi-ROX One-Step Kit (Meridian Biosciences, BIO-73005) on a QuantStudio
602 7 Pro (ThermoFisher). Primer sequences: *NFE2L2* FW, 5'- GAGAGCCCAGTCTTCATTGC-3';
603 *NFE2L2* RV, 5'-TTGGCTTCTGGACTTGGAAC -3'; *RPL19* FW, 5'-GATCCGGAAGCTCATCAAAG -
604 3', *RPL19* RV, 5'-GGCTGTACCCTTCCGCTTAC -3'.
605
606 **Live Cell Imaging**
607 Cells were plated and allowed to attach for 24 hrs before treatment with either vehicle
608 (DMSO, 0.05%), lorlatinib (0.5μM), or alectinib (0.5μM) along with an epigenetic inhibitor if
609 indicated. Culture medium and drugs were changed every 3 days. Sartorius Incucyte 2020
610 was used to take images of each well at least every 3 days, and to analyze the images.
611
612 ***In vivo* metastasis subcutaneous**
613 erALKi expressing mCherry and Parental cells expressing GFP or mCherry a 1:1 mixture of
614 erLor:Parental, erAlec:Parental, or Parental (GFP): Parental (mCherry) in RPMI media. Type
615 3 matrigel was added to each sample in equal volume to the media. The mice were
616 anesthetized with 4% isoflurane for induction, and anesthesia maintenance with 2%

617 isoflurane. 100ul of the cells with matrigel were injected per flank, with 1 million cells per
618 flank. After 4 weeks, both the subcutaneous tumor site and lungs were harvested for flow
619 cytometry analysis. Xenograft studies were performed in accordance with the guidelines of
620 the Institutional Animal Care and All the xenograft studies were performed per the
621 approved procedures of IACUC protocol IS00013344 of the H. Lee Moffitt Cancer Center.
622 Animals were maintained under AAALAC-accredited specific pathogen-free housing
623 vivarium and veterinary supervision following standard guidelines for temperature and
624 humidity, with a 12-hour light/12-hour dark cycle.
625
626 ***In vivo* metastasis tail vein**
627 erALKi expressing mCherry and Parental cells expressing nuclear GFP or mCherry were
628 prepared. Once counted, a 1:1 mixture of erLor:Parental, erAlec:Parental, or Parental
629 (GFP): Parental (mCherry) in RPMI media. 100ul of the cell-containing media with 100,000
630 cells per mouse were injected via tail vein. After 4 weeks, the lungs were harvested for flow
631 cytometry analysis.
632
633 ***In vivo* subcutaneous tumors**
634 Aliquots of LAP and HAP cells were prepared with equal volume RPMI media and type 3
635 matrigel. 375,000 cells were injected per flank. Tumors were allowed to grow until
636 palpable, and alectinib 25mg/kg was delivered daily via gavage. Tumor measurements were
637 taken weekly using electronic calipers. Detection threshold is based on inadequate caliper
638 purchase around lesion. After 19 weeks on alectinib, all three mice bearing HAP-tumors,
639 and one mouse bearing LAP tumors were euthanized and tumors were collected. The
640 remaining 3 mice bearing LAP-tumors were placed on a treatment holiday for 10 weeks
641 until tumors enlarged and were then restarted on alectinib 25mg/kg.
642
643 **Tumor digestion and homogenization**
644 Tumors or lungs were digested in RPMI media supplemented with 1 mg/ml collagenase IV
645 (Worthington),1 mg/ml hyaluronidase (Sigma), and 2 mg/ml bovine serum albumin (Fisher
646 Scientific) at 37 °C. After neutralizing with PBS, the tumor solution was filtered with a cell
647 strainer and centrifuged at 1000rpm for 5 minutes. Supernatant was discarded, and cells
648 were either immediately plated for *in vitro* culture, or resuspended in freezing media
649 (40%RPMI complete, 50%FBS, 10%DMSO) and placed in cryovials at - 80 °C.
650
651 **Flow cytometry analysis**
652 Tumors or lungs containing GFP/mCherry mixes were digested in RPMI supplemented with
653 1 mg/ml collagenase IV (Worthington),1 mg/ml hyaluronidase (Sigma), and 2 mg/ml bovine
654 serum albumin (Fisher Scientific) at 37 °C. Pellets were suspended in PBS and 0.1 µg/ml

655 DAPI (Sigma). Percent of population that is mCherry+ and GFP+ was determined using a
656 MACSQuant Flow Cytometer.
657
658 **Plasma luciferase**
659 Gateway cloning (Invitrogen) was used to generate plasmids with pLenti 6.3 backbone
660 (Invitrogen) and C-luciferase (ThermoFisher, cat:16150). JetPrime reagents and protocol
661 (Polyplus) were followed for transfection into HEK-293T packaging cells. Virus-containing
662 supernatant was collected 24-48h after transfection and filtered through 0.45μm filters
663 (Corning). H3122 cells were infected with viral lysate containing polybrene (Santa Cruz
664 Biotechnology) before selection in the appropriate antibiotic. After selection, luciferase
665 expression was checked by collecting 200ul of the conditioned media after 6 hours. The C-
666 luciferase assay was then conducted.
667
668 ***In vivo* luciferase monitoring**
669 LAP, HAP, or Parental cells secreting C-luciferase were prepared for injection such that
670 100,000 cells were injected via tail vein per mouse. Every two weeks, blood from the tail
671 vein of each mouse was collected into ethylenediaminetetraacetic acid (EDTA) -coated
672 tubes (ThermoScientific) and centrifuged at 2000g for 10 minutes. The plasma was
673 collected and diluted at 1:100 with PBS before the C-luciferase assay was conducted.
674
675 **C-Luciferase Assay**
676 Vargulin, cyprindina luciferase (NanoLight Technologies), was prepared in 0.5mg/ml stock
677 in acidified methanol (5ul of 6N HCL per 1ml methanol). A 1:1000 dilution of stock
678 luciferase was prepared in PBS to make working concentrations. In triplicate, 20ul of the
679 conditioned media or diluted plasma sample was plated in a white-walled 96-well plate.
680 The assay was run with 100ul of luciferase added per well with an integration time of 2
681 seconds.
682
683 **Bulk RNA-seq**
684 Duplicate cultures of H3122 parental cells and single-cell derived clones were cultured
685 until 60-70% confluent, then lysed directly by adding RNA lysis buffer. RNA was isolated for
686 parental cells and single-cell clones using an RNAEasy Minikit (Qiagen). Reads were
687 generated using a Novaseq illumina platform at 30,000,000 reads per sample. Alignment
688 was achieved using HiSat2 and the human hg19 reference genome. Normalized reads were
689 obtained from DeSeq2. Additional unsupervised clustering and PCA analysis was
690 performed using R.
691
692 **Gene set enrichment analysis**

693 GSEA was used to determine the gene sets enriched in high, intermediate and low
694 evolvable clones versus parental cell line RNA-seq profiles. We used the MSigDB Hallmark
695 [PMID: 26771021] as the predefined gene sets and performed 10,000 permutations by gene
696 set to determine the p-values. Gene sets with false discovery rate q-value ≤0.25 were
697 considered as significantly enriched.
698
699 **Single cell transcriptome analysis**
700 Data was originally reported in Vander Velde (2020)[11], briefly, cells were exposed to either
701 no treatment (naive), or to 112 days of lorlatinib or alectinib. Approximately 1,000 cells
702 were collected per sample and processed using the 10X Genomics pipeline on the Illumina
703 NextSeq 500 instrument. In this article, the data has been further analyzed by Gini Score.
704
705 **Gini Analysis**
706 Single cell transcriptomic data was analyzed using the "DescTools" and "Seurat" packages
707 on R.
708
709 **ATAC-seq**
710 Duplicate cultures of H3122 parental cells and cell-line derivatives (two clones from each
711 category such as high, intermediate and low adaptability potential clones, and two
712 independently derived erLor and erAlec replicates) were cultured in complete RPMI until
713 60-70% confluent. Cells were collected and frozen. ATAC-sequencing was performed by
714 ActiveMotif for at least 50,000 reads. Usable reads were aligned to the hg38 reference
715 genome. Bioinformatic analysis was done in collaboration with Berkley Gryder using a
716 previously established pipeline which can be found at
717 https://github.com/GryderLab/gryderlab_pipeline. Briefly, ATAC-seq reads were matched
718 with bulk RNA-seq data from the same clone. Motif enrichment analysis was performed
719 using HOMER and biological processes were identified using ToppGene. Biological
720 processes with p-value less than $1x10^{-6}$ were considered significant.
721
722 **Computational Model**
723 The agent-based model (ABM) includes three cell types—sensitive, baseline-plasticity
724 persisters, and high-plasticity persisters—each capable of proliferation and death. Division
725 and death rates depend on treatment status and local environmental conditions
726 (Supplementary Methods). Mutations arise stochastically at division and are assumed
727 beneficial, providing incremental fitness gains toward resistance. Mutations are
728 mechanism-agnostic (genetic or epigenetic) and occur only upon division. Treatment is
729 modeled as a binary, domain-wide perturbation: sensitive cells are fully inhibited and

rapidly decline, while persister populations maintain net-zero growth until resistance mutations appear.

The ABM is implemented on a 10,000-site two-dimensional grid. Agents interact with their local environment through a Moore neighborhood of eight adjacent sites. Initial populations are randomly seeded according to experimentally or theoretically motivated proportions. At each discrete time step, agents update asynchronously following probabilistic rules for division, death, and mutation. Fifty independent stochastic realizations were run to capture variability.

To complement the ABM and isolate the effects of stochasticity and spatial structure, a deterministic ODE model was developed under identical biological assumptions and rate parameters, modeling population-level dynamics with a carrying capacity of 1,000 cells. Python was used for parameter estimation, data processing, visualization, and to implement both the ABM and ODE models. The ODE simulations, being deterministic, were run once per parameter set. All simulation scripts, parameter files, and analysis notebooks are publicly available at https://github.com/mfroid/plasticityModels/. All ABM data is available upon request from the authors. See **Supplemental Methods** for additional information.

Statistical Analyses

Statistical analysis was performed with Prism 10 (GraphPad) or R statistical software. Details of statistical tests are provided in Supplementary Table 1. *p<0.05, **p<0.01, ***p<0.001, and ****p<0.0001.

DATA AND CODE AVAILABILITY

- All simulation scripts, parameter files, and analysis notebooks are publicly available at https://github.com/mfroid/plasticityModels/. All ABM data is available upon request from the authors.
- ATAC-seq data is publicly available at https://www.ncbi.nlm.nih.gov/sra/PRJNA1400308. The previously established analysis pipeline can be found at https://github.com/GryderLab/gryderlab_pipeline.
- CloneTracer and CloneSweeper datasets can be found at https://www.ncbi.nlm.nih.gov/sra/PRJNA1400309.
- Single Cell RNA sequencing data was previously reported in (6) and can be found at https://www.ncbi.nlm.nih.gov/geo/query/acc.cgi?acc=GSE144282.
- Bulk RNA sequencing data can be found at https://www.ncbi.nlm.nih.gov/sra/PRJNA1400309.

- All data reported in this paper are available from the corresponding author upon request.

AUTHOR CONTRIBUTIONS

AM conceived of the project. AB and XA designed and performed wet-lab experiments and data analysis. MF, RBC, and JM, designed and performed *in silico* experiments under the supervision of AM, JC, and DB. JR performed growth rate assays under the supervision of AB and AM. XA generated the bulk RNA-seq samples and performed the analysis. XA performed the Clone Tracer experiment and analyzed it with VT. RV contributed to making the CloneSweeper technology and liaised our use of it. AB performed the CloneSweeper experiment. AB generated the ATAC-seq samples and performed the analysis under the supervision of BG. AB, VT, and AM designed the schematics. AB, VT, and AM wrote the manuscript. JC, DB, AA, and VT made substantial input to the direction, design, and execution of the project. All authors reviewed the manuscript.

ACKNOWLEDGEMENTS

We thank M. Henry for their contribution to the animal work. This work has been supported in part by the Flow Cytometry Core and the Molecular Genomics Core at the H. Lee Moffitt Cancer Center and Research Institute.

REFERENCES

1. Strebhardt, K. & Ullrich, A. Paul Ehrlich's magic bullet concept: 100 years of progress. *Nat. Rev. Cancer* **8**, 473–480 (2008).
2. Reck, M. & Rabe, K. F. Precision Diagnosis and Treatment for Advanced Non–Small-Cell Lung Cancer. *N. Engl. J. Med.* **377**, 849–861 (2017).
3. Huang, L., Jiang, S. & Shi, Y. Tyrosine kinase inhibitors for solid tumors in the past 20 years (2001–2020). *J. Hematol. Oncol.J Hematol Oncol* **13**, 143 (2020).
4. Lung Cancer Survival Rates | 5-Year Survival Rates for Lung Cancer. *American Cancer Society* https://www.cancer.org/cancer/types/lung-cancer/detection-diagnosis-staging/survival-rates.html.
5. Ramos, P. & Bentires-Alj, M. Mechanism-based cancer therapy: resistance to therapy, therapy for resistance. *Oncogene* **34**, 3617–3626 (2015).
6. Shaffer, S. M. *et al.* Rare cell variability and drug-induced reprogramming as a mode of cancer drug resistance. *Nature* **546**, 431–435 (2017).
7. Marine, J.-C., Dawson, S.-J. & Dawson, M. A. Non-genetic mechanisms of therapeutic resistance in cancer. *Nat. Rev. Cancer* **20**, 743–756 (2020).
8. Sharma, S. V. *et al.* A Chromatin-Mediated Reversible Drug-Tolerant State in Cancer Cell Subpopulations. *Cell* **141**, 69–80 (2010).
9. Nguyen, A., Yoshida, M., Goodarzi, H. & Tavazoie, S. F. Highly variable cancer subpopulations that exhibit enhanced transcriptome variability and metastatic fitness. *Nat. Commun.* **7**, 11246 (2016).

10. Pérez-González, A., Bévant, K. & Blanpain, C. Cancer cell plasticity during tumor progression, metastasis and response to therapy. *Nat. Cancer* **4**, 1063–1082 (2023).
11. Vander Velde, R. *et al.* Resistance to targeted therapies as a multifactorial, gradual adaptation to inhibitor specific selective pressures. *Nat. Commun.* **11**, 2393 (2020).
12. França, G. S. *et al.* Cellular adaptation to cancer therapy along a resistance continuum. *Nature* **631**, 876–883 (2024).
13. Scarborough, J. A. *et al.* Identifying States of Collateral Sensitivity during the Evolution of Therapeutic Resistance in Ewing's Sarcoma. *iScience* **23**, (2020).
14. Fukuda, K. *et al.* Epithelial-to-Mesenchymal Transition Is a Mechanism of ALK Inhibitor Resistance in Lung Cancer Independent of ALK Mutation Status. *Cancer Res.* **79**, 1658–1670 (2019).
15. Deng, S. *et al.* Ectopic JAK–STAT activation enables the transition to a stem-like and multilineage state conferring AR-targeted therapy resistance. *Nat. Cancer* **3**, 1071–1087 (2022).
16. Byers, L. A. *et al.* An Epithelial–Mesenchymal Transition Gene Signature Predicts Resistance to EGFR and PI3K Inhibitors and Identifies Axl as a Therapeutic Target for Overcoming EGFR Inhibitor Resistance. *Clin. Cancer Res.* **19**, 279–290 (2013).
17. Zhang, Z. *et al.* Activation of the AXL kinase causes resistance to EGFR-targeted therapy in lung cancer. *Nat. Genet.* **44**, 852–860 (2012).
18. Holohan, C., Van Schaeybroeck, S., Longley, D. B. & Johnston, P. G. Cancer drug resistance: an evolving paradigm. *Nat. Rev. Cancer* **13**, 714–726 (2013).
19. Jiang, C. *et al.* Innate immunity and the NF-κB pathway control prostate stem cell plasticity, reprogramming and tumor initiation. *Nat. Cancer* 1–22 (2025) doi:10.1038/s43018-025-00994-3.
20. Cammareri, P. *et al.* Loss of colonic fidelity enables multilineage plasticity and metastasis. *Nature* 1–10 (2025) doi:10.1038/s41586-025-09125-5.
21. Lee, J. H. *et al.* TGF-β and RAS jointly unmask primed enhancers to drive metastasis. *Cell* **187**, 6182-6199.e29 (2024).
22. Xu, J., Lamouille, S. & Derynck, R. TGF-β-induced epithelial to mesenchymal transition. *Cell Res.* **19**, 156–172 (2009).
23. Yeh, H.-W. *et al.* PSPC1 mediates TGF-β1 autocrine signalling and Smad2/3 target switching to promote EMT, stemness and metastasis. *Nat. Cell Biol.* **20**, 479–491 (2018).
24. Kim, B. N. *et al.* TGF-β induced EMT and stemness characteristics are associated with epigenetic regulation in lung cancer. *Sci. Rep.* **10**, 10597 (2020).
25. Su, J. *et al.* TGF-β orchestrates fibrogenic and developmental EMTs via the RAS effector RREB1. *Nature* **577**, 566–571 (2020).
26. O'Hagan, S., Wright Muelas, M., Day, P. J., Lundberg, E. & Kell, D. B. GeneGini: Assessment via the Gini Coefficient of Reference "Housekeeping" Genes and Diverse Human Transporter Expression Profiles. *Cell Syst.* **6**, 230-244.e1 (2018).
27. Torre, E. *et al.* Rare Cell Detection by Single-Cell RNA Sequencing as Guided by Single-Molecule RNA FISH. *Cell Syst.* **6**, 171-179.e5 (2018).
28. Estrella, V. *et al.* Acidity Generated by the Tumor Microenvironment Drives Local Invasion. *Cancer Res.* **73**, 1524–1535 (2013).

850 29. Pavlova, N. N., Zhu, J. & Thompson, C. B. The hallmarks of cancer metabolism: Still
851 emerging. *Cell Metab.* **34**, 355–377 (2022).
852 30. Gilmartin, A. G. *et al.* GSK1120212 (JTP-74057) Is an Inhibitor of MEK Activity and
853 Activation with Favorable Pharmacokinetic Properties for Sustained In Vivo Pathway
854 Inhibition. *Clin. Cancer Res.* **17**, 989–1000 (2011).
855 31. Blumenschein, G. R. *et al.* A randomized phase II study of the MEK1/MEK2 inhibitor
856 trametinib (GSK1120212) compared with docetaxel in KRAS-mutant advanced non-
857 small-cell lung cancer (NSCLC). *Ann. Oncol.* **26**, 894–901 (2015).
858 32. Verstovsek, S. *et al.* Safety and Efficacy of INCB018424, a JAK1 and JAK2 Inhibitor, in
859 Myelofibrosis. *N. Engl. J. Med.* **363**, 1117–1127 (2010).
860 33. Li, J., Kim, S. G. & Blenis, J. Rapamycin: One Drug, Many Effects. *Cell Metab.* **19**, 373–
861 379 (2014).
862 34. Lambert, A. W., Zhang, Y. & Weinberg, R. A. Cell-intrinsic and microenvironmental
863 determinants of metastatic colonization. *Nat. Cell Biol.* **26**, 687–697 (2024).
864 35. Combined Use of Tail Vein Metastasis Assays and Real-Time In Vivo Imaging to Quantify
865 Breast Cancer Metastatic Colonization and Burden in the Lungs.
866 https://app.jove.com/v/60687/combined-use-tail-vein-metastasis-assays-real-time-
867 vivo-imaging-to.
868 36. Bhang, H. C. *et al.* Studying clonal dynamics in response to cancer therapy using high-
869 complexity barcoding. *Nat. Med.* **21**, 440–448 (2015).
870 37. Velde, R. J. V., Ng, R. W. S., Coté, C. & Shaffer, S. M. Multiplexed enrichment and
871 tracking of lineages with CloneSweeper. 2026.01.30.700779 Preprint at
872 https://doi.org/10.64898/2026.01.30.700779 (2026).
873 38. Charles, J. P. *et al.* Monitoring the dynamics of clonal tumour evolution in vivo using
874 secreted luciferases. *Nat. Commun.* **5**, 3981 (2014).
875 39. Yue, D. *et al.* Hedgehog/Gli promotes epithelial-mesenchymal transition in lung
876 squamous cell carcinomas. *J. Exp. Clin. Cancer Res.* **33**, 34 (2014).
877 40. Li, D. *et al.* Chromatin Accessibility Dynamics during iPSC Reprogramming. *Cell Stem*
878 *Cell* **21**, 819-833.e6 (2017).
879 41. Buenrostro, J. D., Giresi, P. G., Zaba, L. C., Chang, H. Y. & Greenleaf, W. J. Transposition
880 of native chromatin for fast and sensitive epigenomic profiling of open chromatin, DNA-
881 binding proteins and nucleosome position. *Nat. Methods* **10**, 1213–1218 (2013).
882 42. Takahashi, K. *et al.* Induction of Pluripotent Stem Cells from Adult Human Fibroblasts
883 by Defined Factors. *Cell* **131**, 861–872 (2007).
884 43. Chang, T.-H. *et al.* Slug Confers Resistance to the Epidermal Growth Factor Receptor
885 Tyrosine Kinase Inhibitor. *Am. J. Respir. Crit. Care Med.* **183**, 1071–1079 (2011).
886 44. Guo, W. *et al.* Slug and Sox9 Cooperatively Determine the Mammary Stem Cell State.
887 *Cell* **148**, 1015–1028 (2012).
888 45. Sun, Y., Song, G.-D., Sun, N., Chen, J.-Q. & Yang, S.-S. Slug overexpression induces
889 stemness and promotes hepatocellular carcinoma cell invasion and metastasis.
890 *Oncol. Lett.* **7**, 1936–1940 (2014).
891 46. Moon, J. H., Lee, S. H. & Lim, Y. C. Wnt/β-catenin/Slug pathway contributes to tumor
892 invasion and lymph node metastasis in head and neck squamous cell carcinoma. *Clin.*
893 *Exp. Metastasis* **38**, 163–174 (2021).

894 47. Qian, D. Z. *et al.* Targeting Tumor Angiogenesis with Histone Deacetylase Inhibitors: the
895 Hydroxamic Acid Derivative LBH589. *Clin. Cancer Res.* **12**, 634–642 (2006).
896 48. Ellis, L. *et al.* Histone deacetylase inhibitor panobinostat induces clinical responses
897 with associated alterations in gene expression profiles in cutaneous T-cell lymphoma.
898 *Clin. Cancer Res. Off. J. Am. Assoc. Cancer Res.* **14**, 4500–4510 (2008).
899 49. Shendy, N. A. M. *et al.* Group 3 medulloblastoma transcriptional networks collapse
900 under domain specific EP300/CBP inhibition. *Nat. Commun.* **15**, 3483 (2024).
901 50. Gryder, B. E. *et al.* Histone hyperacetylation disrupts core gene regulatory architecture
902 in rhabdomyosarcoma. *Nat. Genet.* **51**, 1714–1722 (2019).
903 51. Gupta, P. B., Pastushenko, I., Skibinski, A., Blanpain, C. & Kuperwasser, C. Phenotypic
904 Plasticity: Driver of Cancer Initiation, Progression, and Therapy Resistance. *Cell Stem*
905 *Cell* **24**, 65–78 (2019).
906 52. Zeng, Z. *et al.* Reduced chemotherapy sensitivity in EGFR-mutant lung cancer patient
907 with frontline EGFR tyrosine kinase inhibitor. *Lung Cancer* **86**, 219–224 (2014).
908 53. Xu, J. *et al.* Comparison of outcomes of tyrosine kinase inhibitor in first- or second-line
909 therapy for advanced non-small-cell lung cancer patients with sensitive EGFR
910 mutations. *Oncotarget* **7**, 68442–68448 (2016).
911 54. Loria, R. *et al.* Cross-Resistance Among Sequential Cancer Therapeutics: An Emerging
912 Issue. *Front. Oncol.* **12**, (2022).
913 55. Palma, F. R. *et al.* Histone H3.1 is a chromatin-embedded redox sensor triggered by
914 tumor cells developing adaptive phenotypic plasticity and multidrug resistance. *Cell*
915 *Rep.* **43**, 113897 (2024).
916 56. Chakraborty, A. A. *et al.* Histone demethylase KDM6A directly senses oxygen to control
917 chromatin and cell fate. *Science* **363**, 1217–1222 (2019).
918 57. Rolver, M. G. *et al.* Tumor microenvironment acidosis favors pancreatic cancer stem
919 cell properties and in vivo metastasis. *iScience* **28**, (2025).
920 58. Zhang, J., Cunningham, J. J., Brown, J. S. & Gatenby, R. A. Integrating evolutionary
921 dynamics into treatment of metastatic castrate-resistant prostate cancer. *Nat.*
922 *Commun.* **8**, 1816 (2017).
923 59. Smalley, I. *et al.* Leveraging transcriptional dynamics to improve BRAF inhibitor
924 responses in melanoma. *EBioMedicine* **48**, 178–190 (2019).
925

MAIN FIGURES

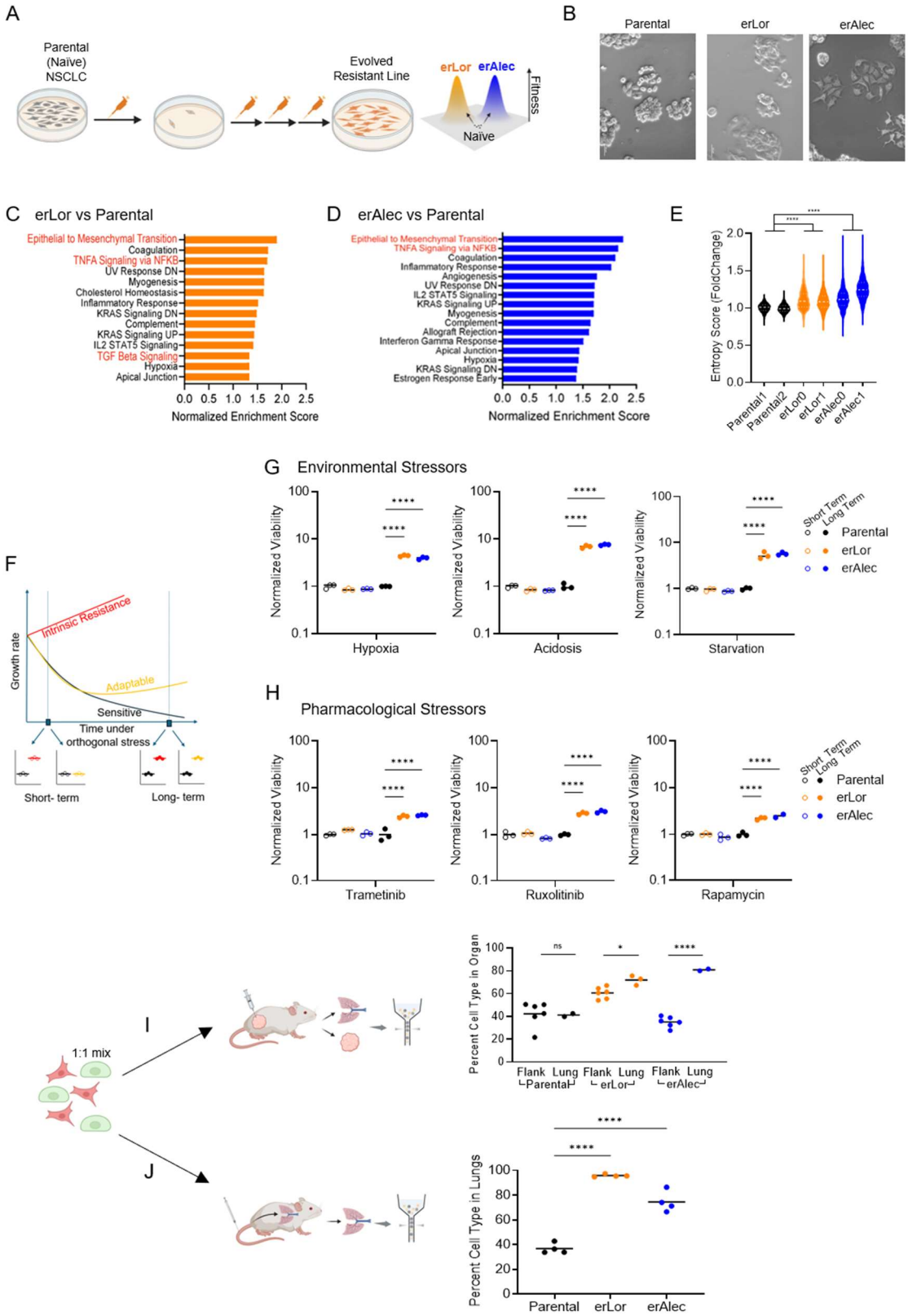

926 **Figure 1. Independent treatment of NSCLC with different TKIs demonstrates**
927 **convergence towards similar resistance phenotypes. A.** Schematic of the experimental
928 design to derive evolved resistant cells to lorlatinib (erLor) and alectinib (erAlec). **B.**
929 Representative bright-field images of Parental, erLor, and erAlec cells in normal media at
930 20x magnification (Scale bar 50μm). **C.** RNA-sequencing analysis of significantly enriched
931 pathways from Gene Set Enrichment Analysis (GSEA) of hallmark gene sets in erLor versus
932 Parental cells or (**D**) erAlec vs Parental cells. Pathways with ≥1.33 normalized enrichment
933 score (NES) shown. **E.** Violin plot of Gini score of transcriptional entropy for RNA
934 sequencing data of two biological replicates each of Parental, erLor, and erAlec. One-way
935 ANOVA with Tukey's multiple comparisons test. **F.** Schematic of expected results of short
936 and long term experiments contrasting intrinsic and acquired resistance. **G.** Quantification
937 of viability staining after short term or long term treatment with environmental conditions
938 hypoxia (200nM $CoCl_2$), acidosis (pH of 5.5), or starvation (1:10 dilution) normalized to
939 growth under normal media. Mean and three replicates shown. Ordinary One-way ANOVA
940 with Tukey's multiple comparisons test was used; only comparisons to the parental sample
941 within each time period are shown. **H.** Quantification of viability staining after short term or
942 long term treatment with trametinib (15nM), ruxolitinib (20μM), or rapamycin (10μM)
943 normalized to vehicle control (DMSO, 0.025%). Mean and three replicates shown. Ordinary
944 One-way ANOVA with Tukey's multiple comparisons test was used; only comparisons to
945 the parental sample within each time period are shown. **I.** Left: schematic of experimental
946 design where mixed populations of Parental GFP cells and mCherry, either erLor or erAlec,
947 cells were injected subcutaneously. Both the primary subcutaneous site and lung
948 metastatic site were collected and cells enumerated via FACS. Right: percent of each cell
949 type found in given organ based on FACS analysis after 27 days post injection. Unpaired t-
950 tests shown. **J.** Left: schematic of experimental design where a mixed populations of
951 Parental GFP+ cells and mCherry+, either erLor or erAlec, cells were injected via tail vein.
952 Right: percent of each cell line found in the lungs after 27 days post injection. One-way
953 ANOVA with Tukey's multiple comparisons test was used; only comparisons to Parental
954 shown.

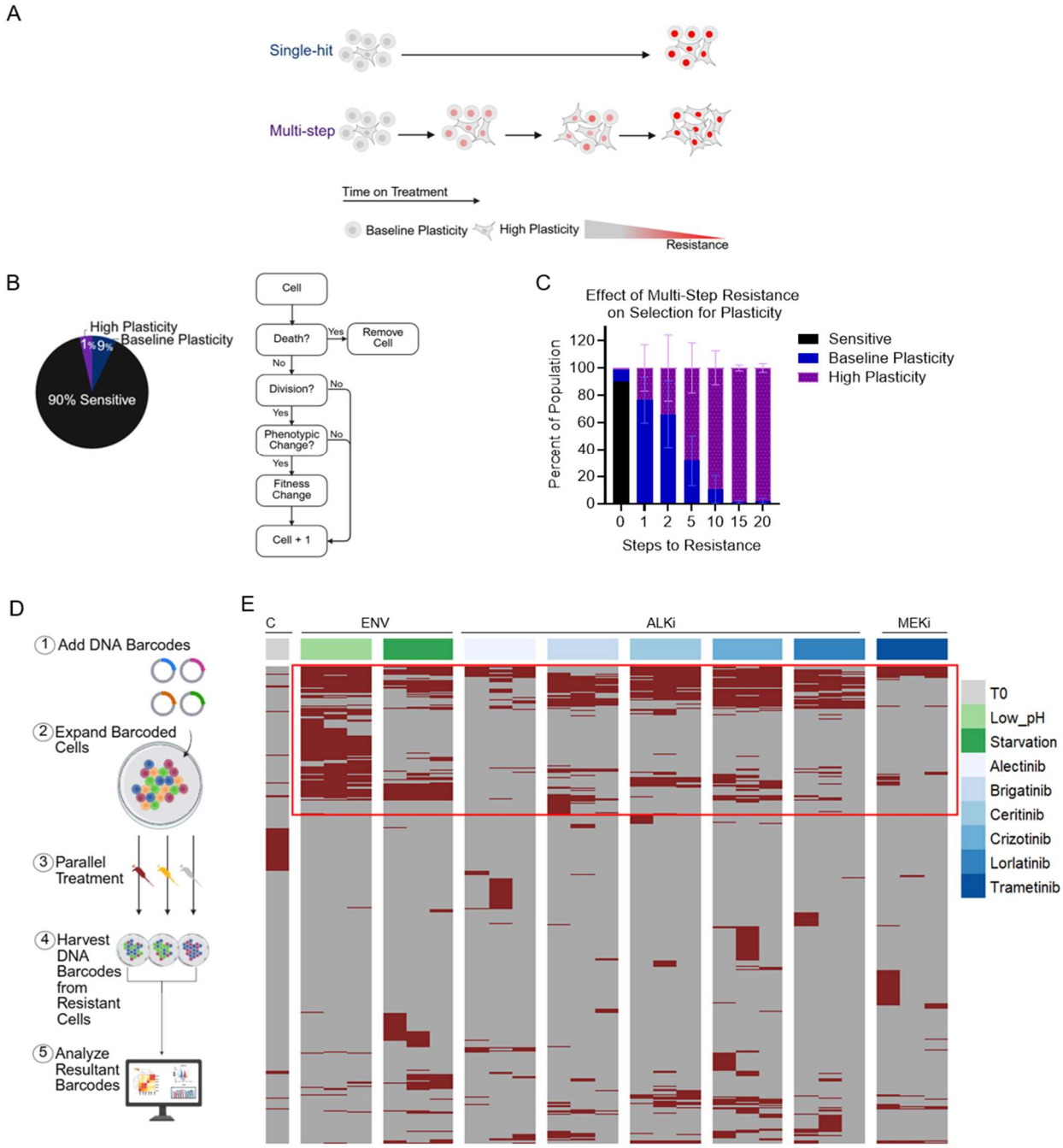

Figure 2. Treatment and exposure to harsh environments drive gradual selection for rare cells with higher adaptability. A. Schematic of hypotheses. **B.** Left: schematic of initial simulation conditions. Right: schematic of agent-based model (ABM) algorithm. **C.** Cell fraction of each population after 600 timesteps based on the number of steps to resistance modeled in each simulation. Mean ± SD shown of 10 simulations. **D.** Schematic of experimental design for barcode libraries. **E.** Unsupervised hierarchical clustering of

961 barcodes from CloneTracer library in each sample based on presence in given treatment.
962 Each row represents a barcode. Each column represents a replicate of a condition. n= 1 for
963 T0, n=3 for all other arms. C = control, T0= time zero, initial time point; ENV = environmental
964 stressor, ALKi= ALK inhibitor, MEKi= MEK inhibitor. DMSO (0.1%), alectinib (0.5μM) lorlatinib
965 (0.5μM), crizotinib (0.5μM), ceritinib (0.1μM), brigatinib (0.1μM), trametinib (0.1μM),
966 Low_pH pH of 6, starvation 1:5 media:PBS.

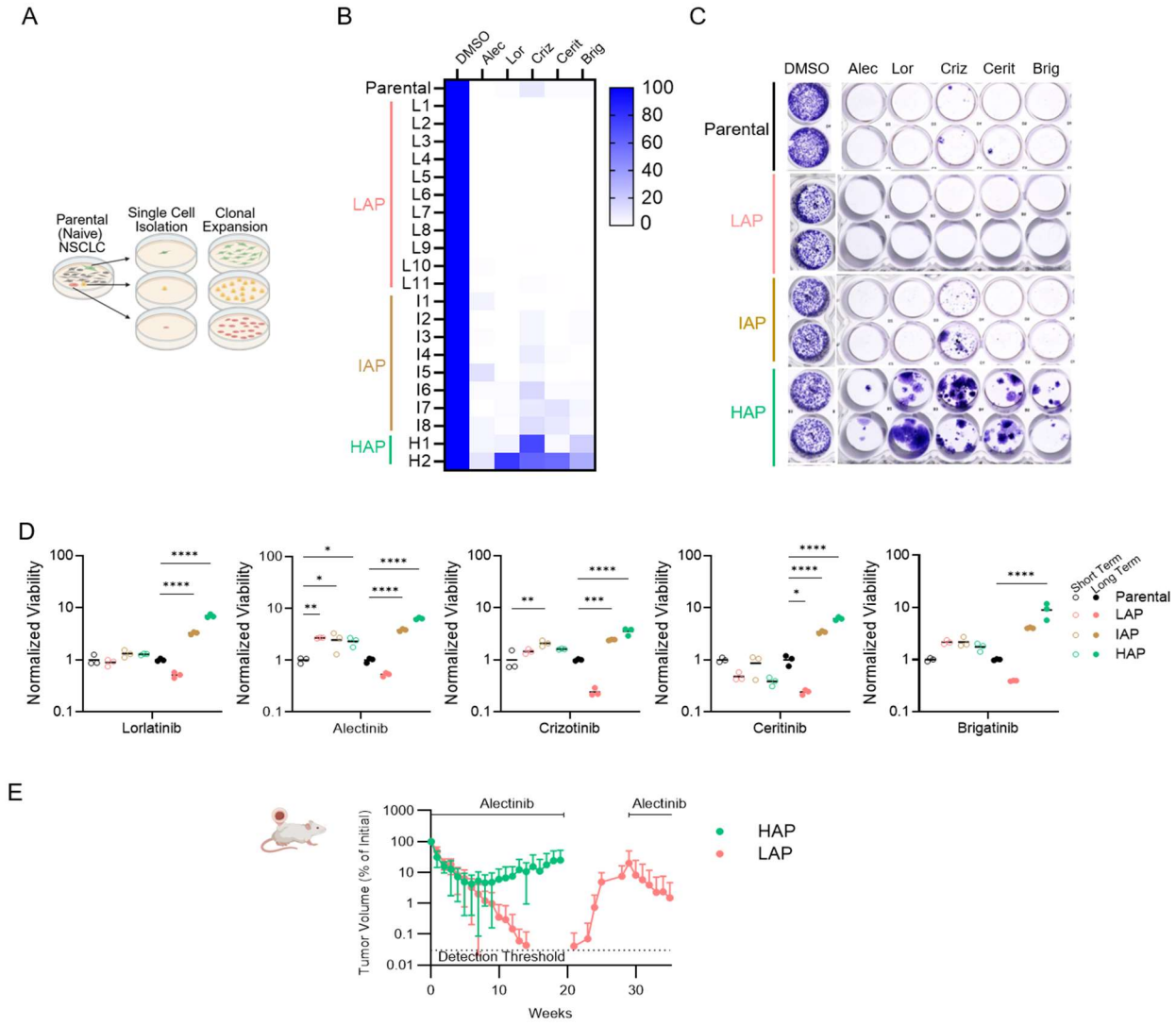

Figure 3. Single-cell-derived clones can be classified into adaptation potentials with distinct functional and molecular profiles. A. Schematic of experimental categorization of single-cell derived clones. **B.** Heatmap representing Image J crystal violet quantification as a percent confluence of each cell line compared to vehicle treatment (DMSO) for up to three months in treatment. Drug treatment displayed as rows, clone number listed as columns for the 21 clones that expanded from single-cell sorting, with final classifications as low, intermediate, or high adaptation-potential. **C.** Crystal violet staining as quantified in Fig. 3B of Parental, HAP, IAP, and LAP cells in DMSO 0.05%, alectinib 0.5μM, lorlatinib 0.5μM, crizotinib 0.5μM, ceritinib 0.1μM, or brigatinib 0.1μM. **D.** Cell Titer Glo quantification of representative clones from each category of LAP, IAP, or HAP. Percent viability after 3 days (short term) or 21 days (long term) normalized to growth under vehicle control. Mean

978 and three replicates shown. Ordinary One-way ANOVA with Tukey's multiple comparisons
979 test was used; only comparisons to the parental sample within each time period are
980 shown. **E.** Volumetric traces of HAP and LAP H3122 xenograft tumors on treatment with
981 25mg/kg alectinib for 20 weeks, followed by a treatment break for LAP tumors for 9 weeks,
982 followed by re-treatment for LAP tumor-bearing mice for 5 weeks. Mean ± SD shown. P
983 values using mixed effect model in Supplementary Table 1 (n= 8 tumors per group).

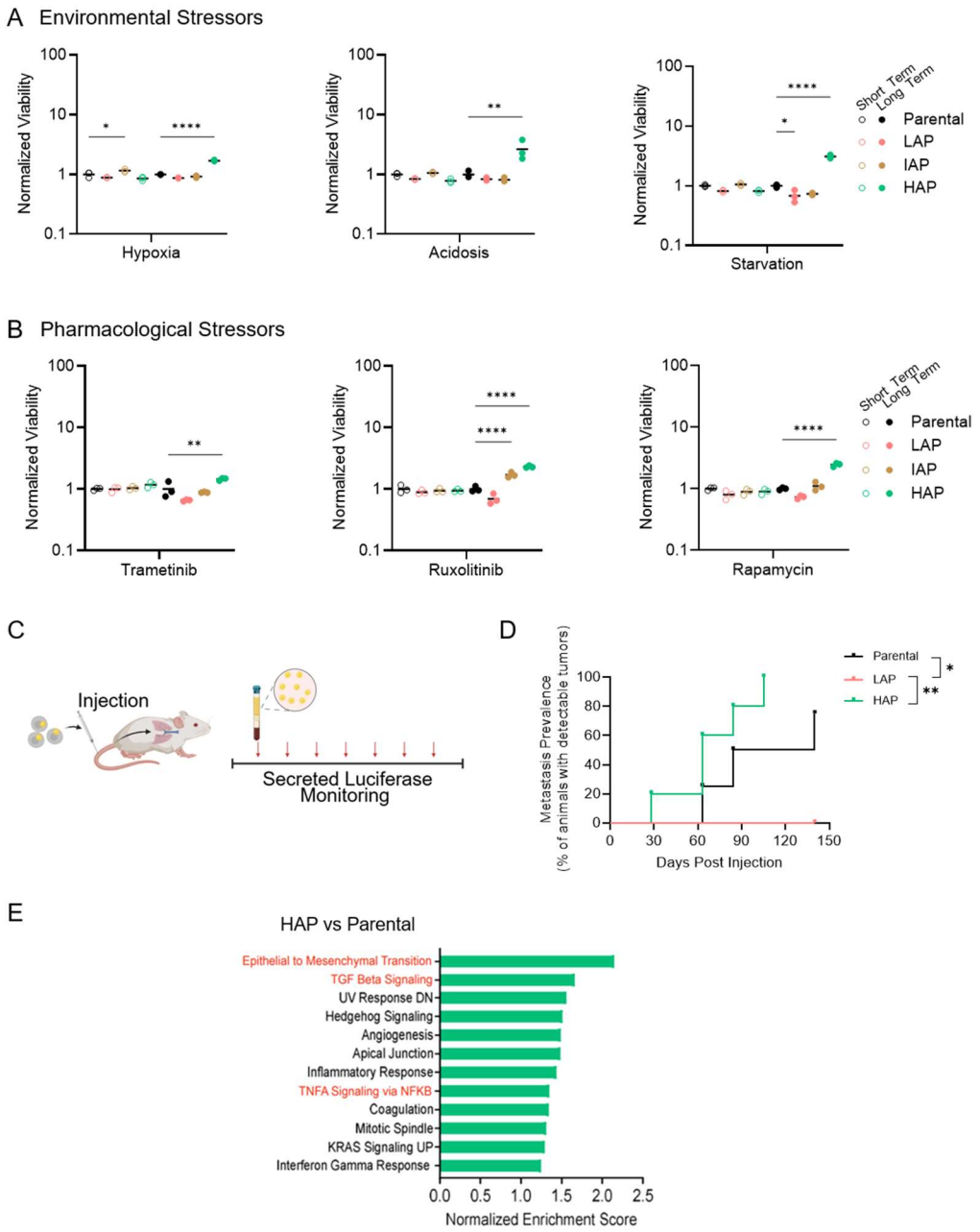

Figure 4. TKI adaptation-potential extends to metastatic potential and multi-stress resistance. **A.** *In vitro* quantification of crystal violet viability staining of representative cell lines of Parental, LAP, IAP, or HAP in hypoxia (200nM $CoCl_2$), acidosis (5.5 pH), or starvation (1:5 media:PBS) normalized to growth under normal media after 3 days (short term) or 16 days (long term). Mean and three replicates (short term) or two replicates (long term) shown. Ordinary One-way ANOVA with Tukey's multiple comparisons test was used; only comparisons to the parental sample within each time period are shown. **B.** *In vitro*

991 quantification of crystal violet viability staining of representative cell lines of Parental, LAP,
992 IAP, HAP, erLor, or erAlec in trametinib (15nM), ruxolitinib (20μM), rapamycin (10μM)
993 normalized to growth under vehicle control (DMSO, 0.025%) after 3 days (short term) or 22
994 days (long term). Mean and three replicates shown. Ordinary One-way ANOVA with Tukey's
995 multiple comparisons test was used; only comparisons to the parental sample within each
996 time period are shown. **C.** Schematic of metastasis experiment with continuous monitoring
997 via luciferase assay of blood plasma. **D.** Cumulative Incidence plot of percent of animals in
998 each group that developed metastasis, as measured by luciferase activity in plasma. n=5
999 for LAP and HAP groups, n=4 for Parental group. Logrank (Mantel-Cox) test shown. **E.**
1000 Significantly enriched pathways from Gene Set Enrichment Analysis (GSEA) of hallmark
1001 gene sets in HAP versus Parental cells from RNA sequencing. Pathways with ≥1.25
1002 normalized enrichment score (NES) shown.

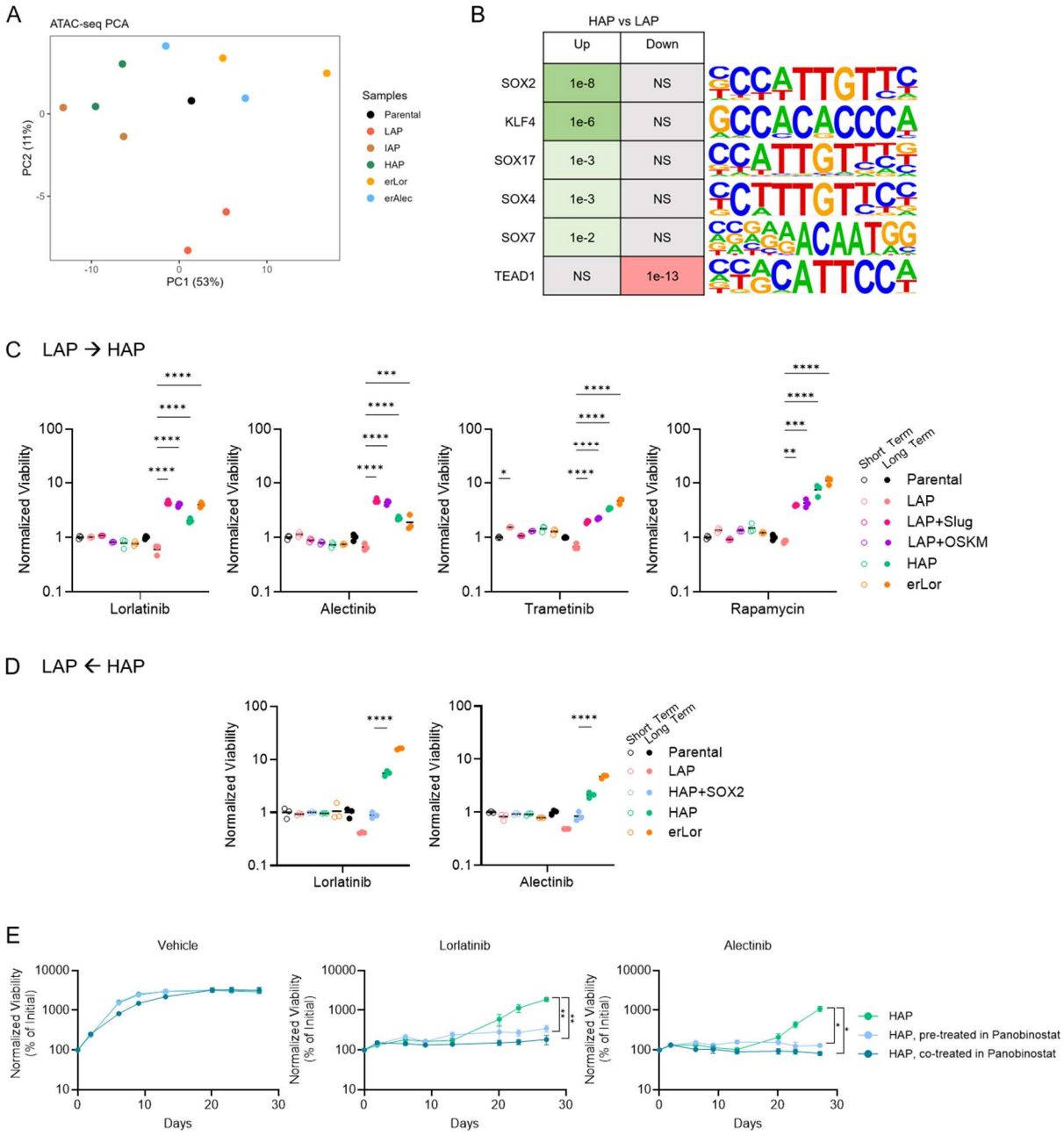

Figure 5. Adaptation-potential can be manipulated. **A.** PCA of top 500 variable genes from bulk ATAC- sequencing. **B.** HOMER known motif enrichment analysis of motifs enriched in HAP cells compared to LAP cells in relevant transcription factors. P -value shown in table. NS, not statistically significant. **C.** Quantification of crystal violet viability staining of Parental, LAP, HAP, LAP + Slug or LAP + OSKM cells in lorlatinib (0.5μM), alectinib (0.5μM), trametinib (15nM), or rapamycin (10μM) normalized to growth in vehicle control (DMSO, 0.025%), after 3 days (short term) or 4 weeks (long term). Mean and three

1010 replicates shown. Ordinary One-way ANOVA with Tukey's multiple comparisons test was
1011 used; only comparisons to the LAP sample within each time period are shown. **D.**
1012 Quantification of crystal violet viability staining of Parental, LAP, HAP, HAP + shSOX2, and
1013 erLor cells in lorlatinib (0.5μM), or alectinib (0.5μM) normalized to vehicle control (DMSO,
1014 0.025%) after 3 days (short term) or 4 weeks (long term). Mean and three replicates shown.
1015 Ordinary One-way ANOVA with Tukey's multiple comparisons test was used; only
1016 comparisons between HAP and HAP+shSOX2 samples within each time period are shown.
1017 **E.** Quantification by live cell imaging of percentage of area covered by cells treated with
1018 vehicle (DMSO, 0.025%; left), lorlatinib (0.5μM; middle), or alectinib (0.5μM; right) with pre-
1019 treatment of co-treatment with Panobinostat (2nM). Two-way ANOVA with repeated
1020 measurements and Tukey's multiple comparison in Supplementary Table 1; comparison to
1021 HAP shown.